Magnetic hydroxyethyl cellulose spheres with efficient congo red removal

Yao Hui
Henan University of Science and Technology

Rukuan Liu
Hunan Academy of Forestry

Qingqing Sun
Henan University of Science and Technology

Liuzemu Li
Hunan Academy of Forestry

Fen Wang
Henan University of Science and Technology

Airong Xu (✉ airongxu@haust.edu.cn)
Henan University of Science and Technology

Zhihong Xiao
Hunan Academy of Forestry

Research Article

Additional Declarations: No competing interests reported.

Magnetic hydroxyethyl cellulose spheres with efficient congo red removal

Yao Hui[a,§], Rukuan Liu[b,§], Qingqing Sun[a], Liuzemu Li[b], Fen Wang[a], Airong Xu[a,*], and Zhihong Xiao[b,*]

[a] School of Chemical Engineering & Pharmaceutics, Henan University of Science and Technology, Luoyang, Henan 471003, P. R. China
[b] State Key Laboratory of Utilization of Woody Oil Resource, Hunan Academy of Forestry, Changsha, Hunan 410004, P. R. China

Correspondence

Airong Xu, PhD

Professor

School of Chemical Engineering & Pharmaceutics,

Henan University of Science and Technology,

Luoyang, Henan 471000, P. R. China

E-mail: airongxu@haust.edu.cn

Zhihong Xiao

Researcher

State Key Laboratory of Utilization of Woody Oil Resource,

Hunan Academy of Forestry,

Changsha, Hunan 410004, P.R. China

E-mail: xzhh1015@126.com

Abstract Ecofriendly adsorbent materials for the rapid and efficient removal of pollutant dyes are highly desired on account of concerns about environmental pollution and human health. Herein, novel magnetic HC/Fe_3O_4 spherical materials have been constructed via crosslinking hydroxyethyl cellulose (HC) by poly(ethylene glycol) diglycidyl ether (PGDE) followed by the introduce of magnetic Fe_3O_4 by a facile and effective strategy developed in this work. The morphology, structure and magnetic behavior of the spherical materials have been systematically investigated using scanning electron microscopy (SEM), X-ray diffraction (XRD), Fourier transform infrared (FT-IR) and vibrating sample magnetometer (VSM) techniques. Further, the spherical materials were utilized to remove congo red ($CR-SO_3Na$) from aqueous solution under varying adsorption conditions. Meanwhile, the adsorption kinetics, thermodynamics and isothermics have been achieved to explore the adsorption process and possible adsorption mechanism of $CR-SO_3Na$ by the spherical materials. The materials show not only an efficient capacity of $CR-SO_3Na$ removal from aqueous solution, but also a sufficient magnetic property of the recovery of the materials from aqueous solution after adsorption. The spherical materials have great potential to be used as efficient adsorbents for the removal of dye-containing effluent.

Keywords: cellulose, magnetic sphere, congo red, adsorption

Introduction

Biomass-based adsorbent materials have increasingly received great attention in water purification industry over the past years because this type of adsorbents are nontoxic and biodegradable unlike conventional petroleum-based adsorbent ones which are harmful to ecological environment and human health due to their extreme difficulty to

be degraded and accumulation in natural environment along with microplastic derived from petroleum-based product wastes (Patel et al. 2018, Law et al. 2014, Rilliing et al. 2012, Roa et al. 2021). Studies have shown that lignocellulosic porous materials prepared from natural biomass corncob and willow wood can remove dye methylene blue and oil from water (Xu et al. 2018). Other lignocellulosic materials applied in the removal of dyes from aqueous solution include jute fiber for anionic-azo (Roy et al. 2012), azadirachta indica leaf powder for anionic-azo (Bhattacharyya et al. 2004), formosa papaya seed powder for crystal violet (Pavan et al. 2014), mustard husk for alizarin red (Gautam et al. 2013), macauba palm cake for methylene blue and congo red (Vieira et al. 2012), agricultural residues wheat straw, corncob and barley husk for cibacron yellow, cibacron red , cibacron blue, remazol black B and remazol red (Robinson et al. 2002).

Cellulose, constantly being produced through photosynthesis, is the most abundant biorenewable resource in the world with outstanding advantages such as availability, low-price, nontoxicity and biodegradability (Hirosawa et al. 2017, Ragauskas et al. 2006, Wang et al. 2012). Over the past years, cellulose has been utilized to fabricate adsorbent composite materials for the removal of toxic dyes from water/wastewater (Roa et al. 2021). However, pure cellulose material displays a low adsorption efficiency for pollutants (Hosseini et al. 2022). To overcome the issue, it is essential that high adsorption capacity components for pollutants are combined with cellulose, or cellulose is modified by functional groups which are able to interact with pollutants. For example, cellulose nanocrystal/graphene oxide nanocomposite (Shi et al. 2014, Zaman et al. 2020), cellulose nanocrystals incorporated with zinc oxide (Oyewo et al. 2020), cellulose nanofibril coated with polydopamine (Huo et al. 2022), and cellulose nanofibril/rectorite composite can be applied as adsorbents for the removal of toxic dye

85   methylene blue from aqueous solution (Chen et al. 2022). The materials of cellulose

86   nanocrystal/microfibril modified by carboxyl groups can adsorb methylene blue (Wu

87   et al.2020, Li et al. 2018), acrylic acid and acrylamide grafted cellulose powders (100

88   mesh) for acid blue 93 and methylene blue (Liu et al. 2015), glycidyl methacrylate and

89   diethylenetriamine pentaacetic acid modified epoxy cellulose for malachite green and

90   basic fuchsine (Zhou et al. 2013), phytic acid and tannin functionalized microcrystalline

91   cellulose for cationic dye (Yuan et al. 2022), polyethyleneimine modified cellulose

92   nanofibers for methyl orange (Zhang et al. 2022), trimethylammonium grafted cellulose

93   for Eosin Y (Feng et al. 2020), ionic liquid modified cellulose for Eosin Y (Wan et al.

94   2019), and Cu(II)-thiourea modified cotton fibers for riochrome cyanine R and 2-(4-

95   sulfo phenyl azo)-1,8 dihydroxy-3,6 naphthalene disulfonic acid (Shafik et al. 2022).

96   In spite of the strong adsorption capacity of these cellulose-based adsorbents for

97   pollutant dyes, their practical applications are often limited. For example, cellulose

98   nanofiber and nanocrystal involve chemicals and complexity in extraction process

99   (Afzal et al. 2021, Siró et al.2010). The modifications of cellulose by some functional

100 groups involves quite complex and time-consuming procedures. In addition, natural

101 cellulose is extremely difficult to be dissolved in water and most of comment solvents,

102 making its practical application be restricted (Xu et al. 2019, Xu et al. 2018).

103   In recent years, some important progress has been made in the application of

104 hydroxyethyl cellulose in the removal of dyes. This is mainly due to the facts that

105 hydroxyethyl cellulose is water-soluble, facilitating it to be functionalized via replacing

106 the hydroxyl hydrogen atoms in hydroxyethyl cellulose (Ding and et al. 2018, Jilal et

107 al. 2018, Chronakis et al. 2002), it is also biocompatible and biodegradable, being a

108 potential candidate of bioadsorbents family for the removal of pollutant dyes (Verma et

109 al. 2021, Al-Shemy et al. 2022). Sultan et al. found that hydroxyethyl cellulose-g-poly

110   (acrylic acid-co-acrylamide)-Fe^{3+}/silver nanoparticles could be empoyled for enhanced

111   adsorption of methylene blue dye (Sultan et al. 2022). lignin-based hydroxyethyl

112   cellulose-PVA absorbents prepared by Huang et al. could efficiently adsorb positively

113   charged dyes such as rhodamine 6G, crystal violet and methylene blue (Huang et al.

114   2019). Gao et al. fabricated hierarchical foam using hydroxyethyl cellulose, silica and

115   graphitic carbon nitride, and they found that the foam exhibited not only a good

116   adsorption capacity towards methylene blue and methyl violet but also high

117   photocatalytic degradation activity towards two dyes (Gao et al. 2022). The

118   investigation of Ayouch et al. indicated that the hydrogel films using hydroxyethyl

119   cellulose and carboxymethyl cellulose as starting materials, and citric acid as a

120   crosslinker could remove methylene blue from aqueous solutions (Ayouch et al. 2021).

121        $CR-SO_3Na$ is a water-soluble anionic benzidine-based diazo dye and extensively

122   applied in textile, paper, paint, pigments, rubber and plastics industries (Helmiyati et al.

123   2022, Debnath et al. 2015). Nevertheless, this dye is non-biodegradable and

124   carcinogenic, thus resulting in causes environmental pollution and human health

125   problems (González-López et al. 2021, Afkhami et al. 2010). Hence, it is vital to

126   remove the dye pollutant from waste water.

127   In this present work, we designed novel and magnetic HC/Fe_3O_4 spheres using HC,

128   PGDE and magnetic Fe_3O_4, which was not reported previously to the best of our

129   knowledge. The spherical materials could be readily fabricated at ambient conditions.

130   PGDE was employed to mainly crosslink HC, and magnetic Fe_3O_4 was introduced into

131   the spherical materials for the convenience of efficient separation of the HC/Fe_3O_4

132   spherical adsorbents from aqueous solutions after adsorptions (Sirajudheen et al. 2020).

133   Further, the spherical materials were used for the adsorption performances of CR-

134   SO_3Na, and batch adsorption experiments were carried out to systematically investigate

the effects of adsorption factors (pH, temperature, dosage, contact time, and initial dye concentration) on the adsorption of the HEC/Fe$_3$O$_4$ spheres towards CR-SO$_3$Na. The adsorption process was investigated using isotherm and thermodynamic and kinetic models to explore possible adsorption mechanism of CR-SO$_3$Na by HEC/Fe$_3$O$_4$. The recovery and the reusability of the HEC/Fe$_3$O$_4$ adsorbents were also estimated.

Materials and methods

Reagents and materials

Congo red (CR-SO$_3$Na, > 98 %), hydroxyethyl cellulose (HC) (5000-6000 mpa • s, 25 °C), tween 80 and liquid paraffin were purchased from Aladdin Biochemical Technology Co., Ltd. Poly(ethylene glycol) diglycidyl ether (PGDE, average M_n 500) was from Aldrich-Sigma. FeCl$_3$·6H$_2$O (≥ 99.0 %) was purchased from Xilong Science Co., Ltd. Ethanol (≥99.5 %) was purchased from Tianjin Deen Chemical Reagent Co., Ltd. FeCl$_2$·4H$_2$O (≥ 99.7 %) was purchased from Tianjin Bailunsi Biotechnology Co., Ltd. All chemicals were used as received. Deionized water was used throughout all the experiments in this paper.

Fabrication of the magnetic HC/PGDE spheres

The magnetic HC/PGDE spheres were fabricated using the following procedure. A HC aqueous solution was obtained by dissolving 0.48 g of HC in 15.2 g of deionized water. To this HC aqueous solution, NaOH was added under stirring until NaOH was completely dissolved to gain a HC/NaOH solution. At this time, 0.96 g of PGDE was add to the HC/NaOH solution, stirring for 10 min at ambient temperature to gain a HC/PGDE/NaOH solution.

87.6 g of paraffin was mixed with 17.8 g of Tween 80 under stirring to gain a liquid

158 paraffin/Tween 80 mixture. Then, the HC/PGDE/NaOH solution was dropwise added

159 to this mixture under fiercely stirring. After the addition of the HC/PGDE/NaOH

160 solution was completed, continuously stirring for 4 h. Finally, the HC/PGDE spheres

161 were washed by water and ethanol, and then immersed in ethanol to remove water in

162 the spheres.

163 $\qquad$ FeCl$_3$·6H$_2$O and FeCl$_2$·4H$_2$O were added to deionized water, stirred for 10 min,

164 heated to 70 °C and then cooled to ambient temperature to a Fe^{3+}/Fe^{2+} solution. The

165 whole process was protected by nitrogen to prevent Fe^{2+} from being oxidized. In this

166 solution, the molar ratio of Fe^{3+} to Fe^{2+} is 2, and the total concentration of Fe^{3+} and Fe^{2+}

167 is 0.3 mol·L^{-1}. The HC/PGDE spheres fabricated above were immersed in the Fe^{3+}/Fe^{2+}

168 solution for 3 h. The unabsorbed Fe^{3+}/Fe^{2+} solution was poured out. Then, the

169 HC/PGDE spheres which adsorbed the Fe^{3+}/Fe^{2+} solution were immersed in NaOH

170 solution of 0.5 mol·L^{-1} for 1 h to obtain wet magnetic HC/PGDE hydrogel spheres.

171 After being washed with deionized water, the wet spheres were freeze-dried to obtain

172 dried magnetic HC/PGDE spherical samples.

173 **Characterization of the magnetic HC/PGDE**

174 The chemical groups of the magnetic HC/PGDE were analyzed by IR measurement (4

175 cm^{-1} resolution and 64 scans) in the range of 400 − 4000 cm^{-1}, each sample was

176 prepared into thin slice using KBr before determination.

177 $\qquad$ The morphology of the fracture surface of the magnetic HC/PGDE was observed

178 on a scanning electron microscope, the dried magnetic HC/PGDE film was frozen by

179 liquid nitrogen and snapped immediately, prior to the observation, samples were

180 sputtered with gold.

181 $\qquad$ X-ray diffraction (XRD) was recorded on A BrukerD8Advance diffraction

182 spectrometer with Cu-Ka radiation (40 kV, 2° min^{-1}, λ = 1.54 Å), the determined 2θ

183 range was 5–60°.

Adsorption investigation of CR-SO₃Na

185 Batch adsorption investigations were completed using the HC/PGDE as a adsorbent to

186 remove CR-SO₃Na from an aqueous CR-SO₃Na solution. The following adsorption

187 factors were investigated including contact time, solution pH, temperature, adsorbent

188 dose and initial CR-SO₃Na concentration. The contact time investigations were

189 completed at time = 0 − 120 min and a fixed initial CR-SO₃Na concentration of 100

190 mg L^{-1}, adsorbent dosage of 0.5 g L^{-1} and 30 °C. The pH investigations were completed

191 at pH = 2 − 6 and a fixed initial CR-SO₃Na concentration of 100 mg L^{-1}, adsorbent

192 dosage of 0.5 g L^{-1} and 30 °C for 20 h. The temperature investigations were completed

193 at temperature = 25 − 45 °C and a fixed initial CR-SO₃Na concentration of 100 mg L^{-1}

194 and adsorbent dosage of 0.5 g L^{-1} for 20 h. The adsorbent dose investigations were

195 completed at adsorbent dose = 0.1− 1.2 g L^{-1} and a fixed initial CR-SO₃Na

196 concentration of 100 mg L^{-1} and 30 °C for 20 h. The initial CR-SO₃Na concentration

197 investigations were completed at concentration = 25 − 300 mg L^{-1} and a fixed adsorbent

198 dosage of 0.5 g L^{-1} and 30 °C for 20 h. For the contact time, temperature, adsorbent

199 dose and initial CR-SO₃Na concentration investigations, the pH refer to the pH of

200 aqueous CR-SO₃Na solution.

201   Each experiment was repeated three times and the averages values were calculated.

202 The adsorption capacity (q) and removal efficiency (R_e) of each dye were calculated

203 using the following Eq. 1-3:

204

205

$$q_e = \frac{C_0 - C_e}{m} \times V \tag{1}$$

$$q_t = \frac{(C_0 - C_t) \times V}{m} \tag{2}$$

$$R_e = \frac{C_0 - C_t}{C_0} \times 100 \,\% \tag{3}$$

Where, q_e (mg g^{-1}) and q_t (mg g^{-1}) are the equilibrium adsorption capacity and adsorption capacity at time t, respectively. C_0, C_e and C_t were the initial, equilibrium and time t dye concentrations (mg L^{-1}), respectively. m (g) and V (L) were the mass of HC/PGDE and the volume of the dye solutions, respectively.

Results and discussion

Preparation strategy of the magnetic HC/Fe₃O₄

The recovery and reuse of the adsorbents after adsorption towards dye pollutants are of significance in terms of their practical application. Moreover, the magnetic HC/Fe$_3$O$_4$ spheres prepared in this work are primarily utilized in removing CR-SO$_3$Na from aqueous solution. Therefore, Fe$_3$O$_4$ was introduced into the HC/Fe$_3$O$_4$ spheres for the convenience of its separation from aqueous solution after adsorption towards CR-SO$_3$Na. Meanwhile, our previous investigations found that the adsorbents prepared from higher biomass concentration could result in the decreased removal efficiency for pollutant dyes (Xu et al. 2018). Thus, the concentration of HC was selected as low as possible, similarly for NaOH solution concentration and PGDE/HC mass ratio to reduce the amounts of NaOH and PGDE needed to prepare the HC/Fe$_3$O$_4$. Based on this conception, the concentration of HEC was selected at 3 wt%, 5 wt% for NaOH solution concentration and 2 for PGDE/HEC mass ratio. In the light of the above preparation

231   strategy, the magnetic HC/Fe_3O_4 spheres were readily prepared at ambient temperature:

232   The HC/PGDE/NaOH solution was dropwise added to a paraffin/Tween 80 mixture

233   under fiercely stirring, and simultaneously HC was crosslinked by PGDE in this process

234   to gain gel spheres (see Fig. 1a), the spheres were successively washed by water and

235   ethanol, and then immersed in ethanol to remove water in the spheres, the water−free

236   spheres were immersed in a Fe^{3+}/Fe^{2+} solution for 3 h to introduce magnetic Fe_3O_4

237   followed by being washed by deionized water and subsequently freeze-dried to obtain

238   dried magnetic HC/PGDE spheres (see Fig. 1b).
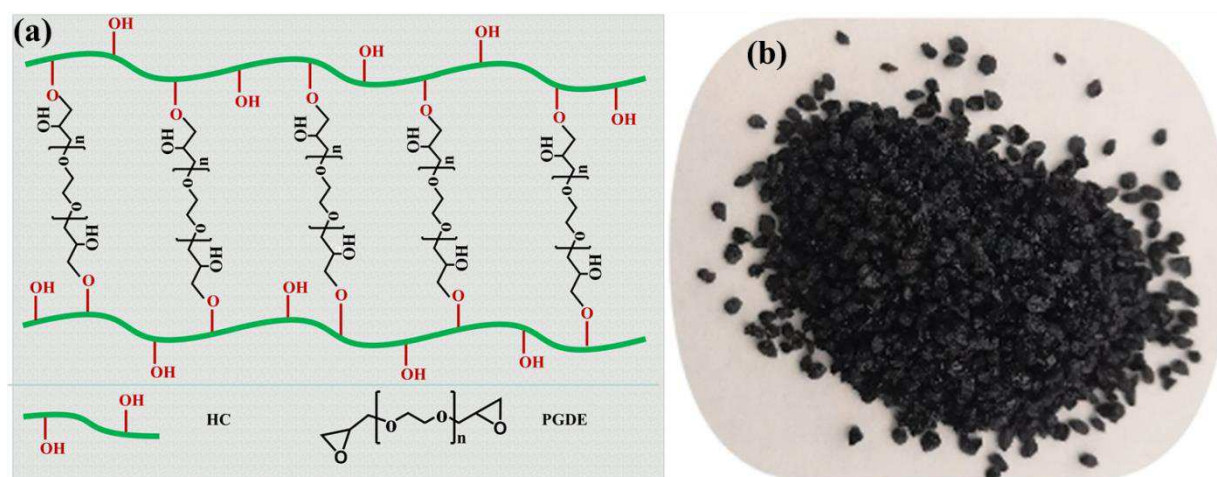
239

240   **Fig. 1** Schematic diagram of the HC crosslinked by PGDE (a), electronic photo of the magnetic

241   HC/Fe_3O_4 spheres (b).

242   **Morphology and magnetic property for the HC/Fe_3O_4**

243   Figure 2 depicts the SEM observation of the fracture and pore wall surfaces of the

244   magnetic HC/Fe_3O_4. Obviously, the magnetic HC/Fe_3O_4 presents a fluffy and porous

245   microstructure, and its pores are composed of randomly oriented HC/Fe_3O_4 walls (Fig.

246   2a), which is similar to the cellulose materials prepared using functionalized

247   imidazolium carboxylate ionic liquids (Xu et al. 2018, Xu et al. 2020), and aqueous

248   NaOH/thiourea solution (zhang et al. 2002). Such fluffy and porous structure is

249 beneficial to dye molecules (Xu et al. 2018). This porous structure mainly results from

250 the fact that during the freezing process in a refrigerator, the water in the wet HC/Fe_3O_4

251 gels was frozen into solid (ice), and the HC/Fe_3O_4 were squeezed into sheets, after the

252 ice sublimation during freeze-dring process, the HC/Fe_3O_4 porous materials with fluffy

253 and porous morphological structures were formed.
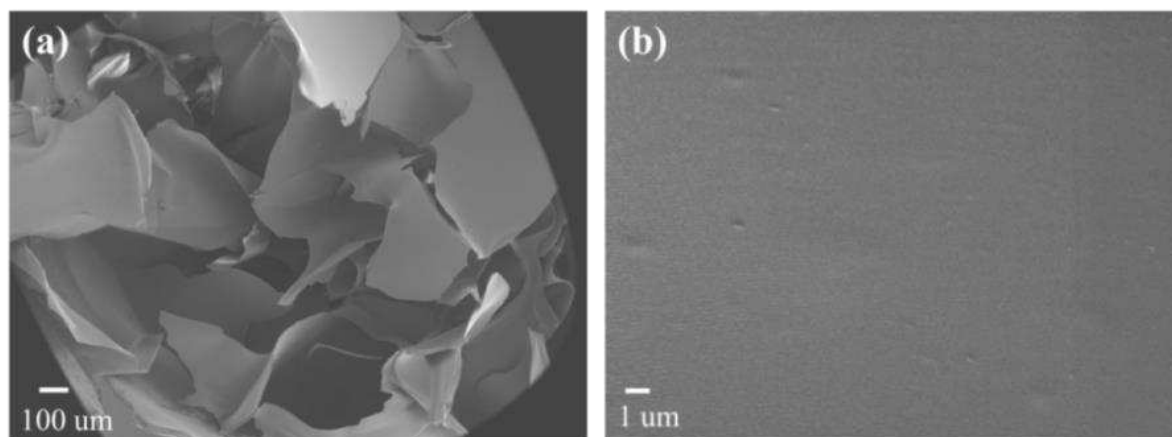
254

255 **Fig. 2 a** SEM images of the magnetic HC/Fe_3O_4, **b** Section, pore wall
256
257
258   The magnetic property of the HC/Fe_3O_4 was recorded using VSM at room

259 temperature, as presented in Figure 3. The saturated magnetization of the HC/PGDE is

260 26.4 $emu \cdot g^{-1}$, indicating that its magnetic property is sufficient for the magnetic

261 separation of HC/Fe_3O_4 from aqueous solution (see the inset of the bottom right of Fig.

262 3). In addition, almost zero residual magnetic susceptibility is observed, indicating that

263 the HC/Fe_3O_4 sample is superparamagnetic.
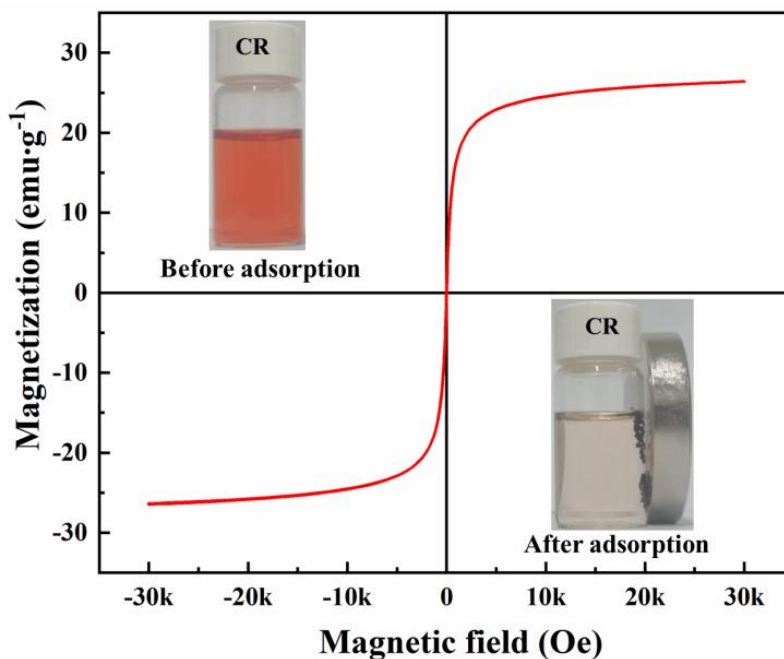
**XRD and FT-IR analysis of the magnetic HC/PGDE**

The XRD spectra of the HC/Fe$_3$O$_4$ and original HEC are shown in Fig. 4a. The obvious

diffraction peak at 2θ value of 20° is an indicative of the (002) reflection of the original

HEC. A weaker peak at 2θ value of 35.5° is ascribed to the (311) reflection of Fe$_3$O$_4$ of

the HC/Fe$_3$O$_4$ (Eltaweil et al. 2020), suggesting that Fe$_3$O$_4$ has been successfully

incorporated during fabrication process. It is also found that no diffraction peak

corresponded to the HC appears for the HC/Fe$_3$O$_4$. This mainly results from the

crosslinking reaction of PGDE with the hydroxyl of HC, leading to the disappearance

of the diffraction peak ascribed to the HC.

Fig. 4b shows the IR spectra of the HC/Fe$_3$O$_4$ and original HEC. The spectra of

the HC feature a wide O-H stretching vibration at 3500−3000 cm^{-1}, C-H asymmetric

and symmetric stretching vibrations at 2919, 2878 cm^{-1}, a C-O-H plane vibration at

1352 cm^{-1}, a C-O-C stretching vibration at 1056 cm^{-1}, which are the characteristics of

the HC (Fan et al. 2016). As shown in Fig. 4b, the peaks attributed to the HC are

significantly decreased or disappeared in the HC/Fe$_3$O$_4$ IR spectra, revealing a

crosslinking reaction of PGDE with the hydroxyl of the HC which is consistent with

the XRD findings discussed above. At the same time, this also indicates that for the

magnetic HC/Fe$_3$O$_4$, PGDE mainly serves to crosslink the hydroxyl of HC.
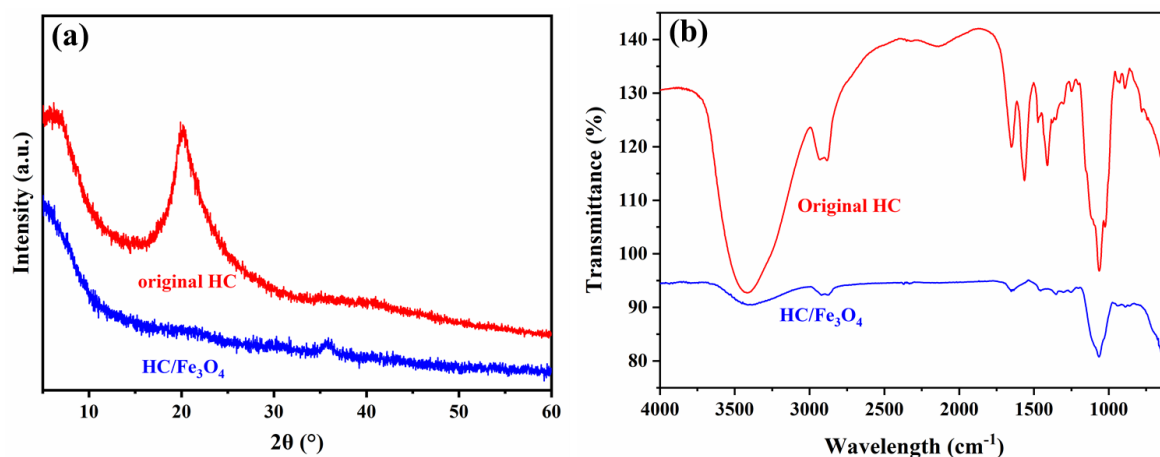
**Fig. 4 a** XRD diffraction peaks and **b** FT-IR spectra of HC and HC/Fe$_3$O$_4$

Effects of Solution pH and adsorbent dose on CR-SO$_3$Na Adsorption

The effect of solution pH on CR-SO$_3$Na adsorption is shown in Fig. 5a. It is evident

that the adsorption of CR-SO$_3$Na is significantly impacted by solution pH. The

adsorption capacity of the HC/Fe$_3$O$_4$ towards CR-SO$_3$Na reduces with the rise of pH.

This primarily results from the following facts: CR-SO$_3$Na is an anionic dye which can

be dissociated into CR-SO$_3^-$ anion and Na$^+$ cation in water, the protonated hydroxy

groups in the HC/Fe$_3$O$_4$ under acidic condition generate a electrostatic attraction

towards the anion of CR-SO$_3$Na, with increasing pH, the deprotonated hydroxy groups

gradually disable the electrostatic attraction of the HC/Fe$_3$O$_4$ towards the anion.

Fig. 5b shows dosage effect on CR-SO$_3$Na adsorption. The removal efficiency of

the HC/Fe$_3$O$_4$ for CR-SO$_3$Na considerably increases with increasing dosage. This is

mainly because the more the amount of the dosage is, the more the available adsorption sites for CR-SO$_3$Na adsorption also is. However, the equilibrium adsorption capacities of the HC/Fe$_3$O$_4$ for CR-SO$_3$Na decrease with adsorbent dosage. This is mainly due to the fact that with the increase of dosage, the non-adsorbed sites in the HC/Fe$_3$O$_4$ become more and more, thus leading to the decreased adsorption capacity.
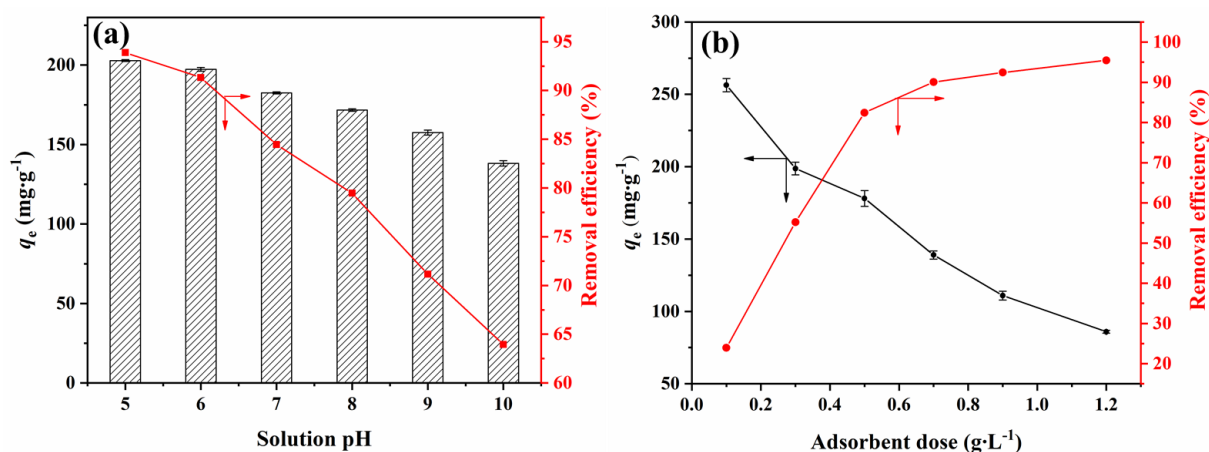

Fig. 5 a Adsorption capacity and removal efficiency vs. solution pH, **b** Adsorption capacity and removal efficiency vs. adsorbent dose

Adsorption time effect and kinetics

The dependence of the adsorption capacity of on time is presented in Fig. 6a. At the initial stage of adsorption, the adsorption capacity of the HC/Fe$_3$O$_4$ for CR-SO$_3$Na enhances rapidly with time. This is mainly due to a large amount of available vacant adsorptive sites on the HC/Fe$_3$O$_4$, being to the benefit of CR-SO$_3$Na adsorption. With an elongation in time, vacant sites on the HC/Fe$_3$O$_4$ are gradually occupied by CR-SO$_3$Na molecules, and it takes a long time for CR-SO$_3$Na molecules to be adsorbed on the vacant sites of the HC/Fe$_3$O$_4$, thus resulting in a decreased adsorption rate. At the last adsorption stage, the adsorption equilibrium achieves, and thus keep hardly variable adsorption rate.
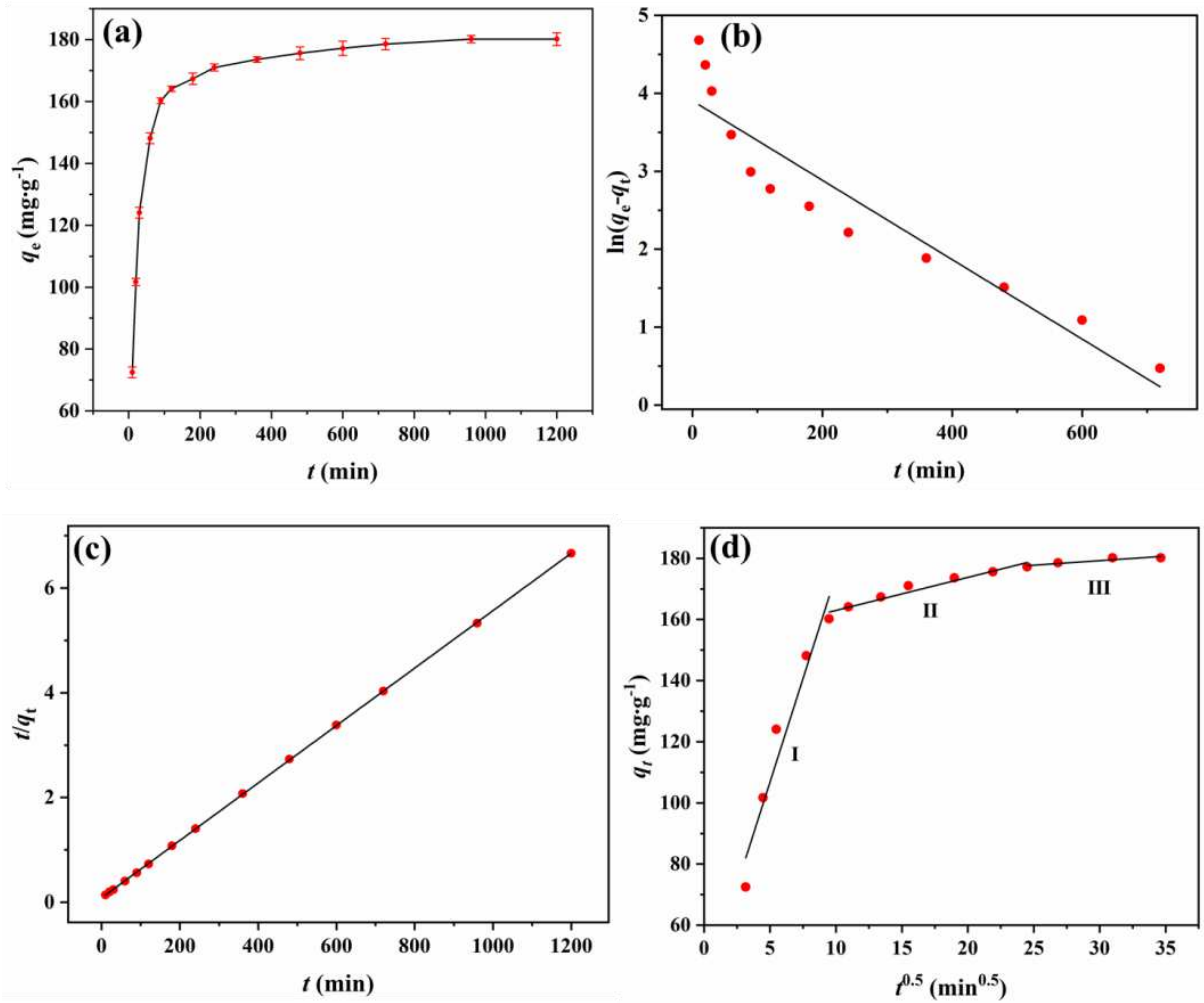
Fig. 6 a q_e variation of the HC/Fe$_3$O$_4$ towards CR-SO$_3$Na with time, **b** Pseudo-first-order kinetic fitting curve, **c** pseudo-second-order kinetic fitting curve, **d** intraparticle diffusion fitting curve

The pseudo-first-order (Eq. 4) and pseudo-second-order (Eq. 5) models are used to investigate the adsorption process of CR-SO$_3$Na by the HC/Fe$_3$O$_4$ (Fan et al. 2016, Deng et al. 2013).

$$\ln(q_e - q_t) = \ln q_e - K_1 t \tag{4}$$

$$\frac{t}{q_t} = \frac{1}{K_2 q_e^2} + \frac{t}{q_e} \tag{5}$$

The adsorption kinetic curves of CR-SO$_3$Na on the HC/Fe$_3$O$_4$ based on the pseudo-first-order and pseudo-second-order model equations are shown in Fig. 6 b and c, respectively, and the fitted parameters using the two equations are summarized in Table

1. The pseudo-first-order kinetic correlation coefficients ($R^2 = 0.88826$) for the adsorptions of CR-SO$_3$Na by the HC/Fe$_3$O$_4$ is much less than the pseudo-second-order kinetic correlation coefficients ($R^2 = 0.99997$). Moreover, the adsorption capacity ((q_e)$_{cal}$ = 182.48 mg g^{-1}) calculated using the pseudo-second-order kinetic equation is extremely closer to the experimentally determined value ((q_e)$_{exp}$ = 180.16 mg g^{-1}). However, the adsorption capacity ((q_e)$_{cal}$ = 49.62 mg g^{-1}) calculated by the pseudo-first-order kinetic equation is much less than the experimental value ((q_e)$_{exp}$ = 180.16 mg g^{-1}). Thus, the pseudo-second-order kinetic model is more proper to describe the adsorption of CR-SO$_3$Na by the HC/Fe$_3$O$_4$ than the pseudo-first-order kinetic model, suggesting that the adsorption of CR-SO$_3$Na by the HC/Fe$_3$O$_4$ are primarily chemisorption (Wang et al. 2020).

Table 1 Kinetic parameters of the adsorptions of CR-SO$_3$Na by the HC/Fe$_3$O$_4$

Models	(q_e)$_{exp}$ (mg g^{-1})	Parameters		R^2
Pseudo-first-order	180.16	K_1 (h^{-1}) 5.09×10^{-3}	(q_e)$_{cal}$ (mg g^{-1}) 49.62	0.88826
Pseudo-second-order	180.16	K_2 (g mg^{-1} h^{-1}) 3.60×10^{-5}	(q_e)$_{cal}$ (mg g^{-1}) 182.48	0.99997
Intraparticle diffusion		K_{dif1} (mg g^{-1} min$^{-1/2}$) 13.52	C_1 39.2547	0.94408
		K_{dif2} (mg g^{-1} min$^{-1/2}$) 1.08	C_2 152.157974	0.94611

The adsorption kinetic data were further analyzed with the intraparticle diffusion kinetic (Eq. 6) model to identify the diffusion mechanism during an adsorption process (Xu et al. 2022). The fitted curve and parameters using this equation are shown in Fig. 6d and Table 1, respectively.

$$q_t = K_{difi}t^{0.5} + C \tag{6}$$

As seen in Fig. 6d, the curve of intra particle diffusion includes three linear sections. The first linear section of the curve with a large slope associates with the diffusion adsorption caused by the diffusion of CR-SO$_3$Na through the solution to the

360   external surface of the HC/Fe$_3$O$_4$. The second linear section is related to the gradual

361   adsorption stage resulting from the intraparticle diffusion of CR-SO$_3$Na from the

362   exterior surface to the interior of the HC/Fe$_3$O$_4$. The last linear section attributes to a

363   very slow adsorption equilibrium stage, indicating a very slow diffusion of CR-SO$_3$Na

364   of the extremely low CR-SO$_3$Na concentration in the aqueous CR-SO$_3$Na solution into

365   the HC/Fe$_3$O$_4$ (Chaukura et al. 2017).

Initial concentration effect and adsorption isotherm

367   As shown in Fig. 7, initial concentration (C_0) remarkedly effect on adsorption capacity

368   (q_e) and removal efficiency. The adsorption capacity significantly enhances with initial

369   concentration of CR-SO$_3$Na solution. It is easy to understand considering the fact: With

370   a rise in CR-SO$_3$Na initial concentration, the driving capacity of the adsorption of CR-

371   SO$_3$Na molecule onto the adsorption site of the HC/Fe$_3$O$_4$ (Dai et al. 2018). However,

372   the removal efficiency displays a contrary trend with CR-SO$_3$Na initial concentration.

373   This results from the limited vacant adsorption sites on the HC/Fe$_3$O$_4$ which are not

374   enough to absorb more CR-SO$_3$Na molecules at high initial concentration (Chen et al.

375   2019).
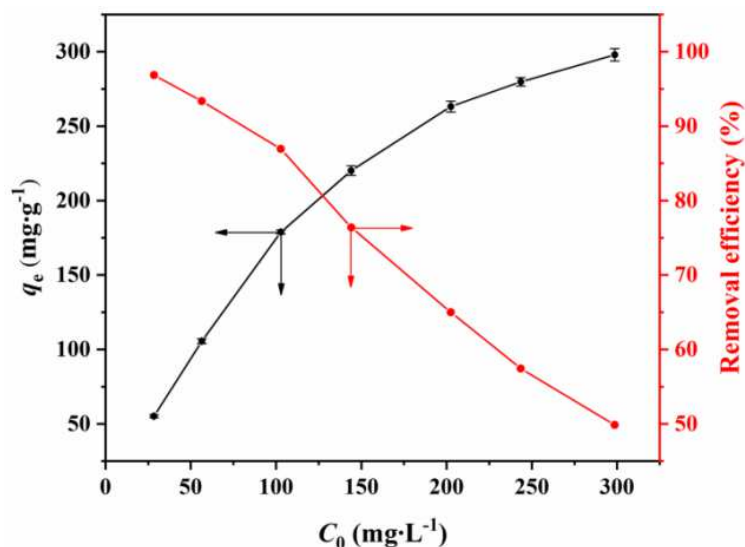
376

377   **Fig. 7** Adsorption equilibrium capacity (q_e) and removal efficiency vs. initial concentration (C_0).

378

379   The interaction between the adsorbent (HC/Fe_3O_4) and adsorbate molecule (CR-

380   SO_3Na) was investigated using the adsorption isotherm models below (Chaukura et al.

381   2017, Ai et al. 2011).

382   Langmuir isothermal model:
383

$$\frac{C_e}{q_e} = \frac{1}{bq_{max}} + \frac{C_e}{q_{max}}$$

384   (9)

385    $$R_L = \frac{1}{1+K_L C_0}$$ (10)

386
387   Freundlich isothermal model:
388

$$\ln q_e = \ln K_F + \frac{1}{n}\ln C_e$$

389   (11)
390

391   In the above equations, q_{max} (mg g^{-1}) is the maximal adsorption capacity, and b (L mg^{-1})

392   for the adsorption intensity or Langmuir coefficient related to the affinity of the binding

393   site, respectively. R_L stands for the separation factor, which is used to judge the degree

394   of adsorption: $R_L = 0$, adsorption does not occur, $R_L > 1$, adsorption is difficult to occur,

395    $0 < R_L < 1$, adsorption is easy to occur. K_F is Freundlich isotherm constant. n is a

396   constant related to the adsorption strength. The larger n is, the stronger the

397   heterogeneity of the material surface is. When n is about 1, meaning that the adsorbent

398   has relatively homogeneous binding sites.

399
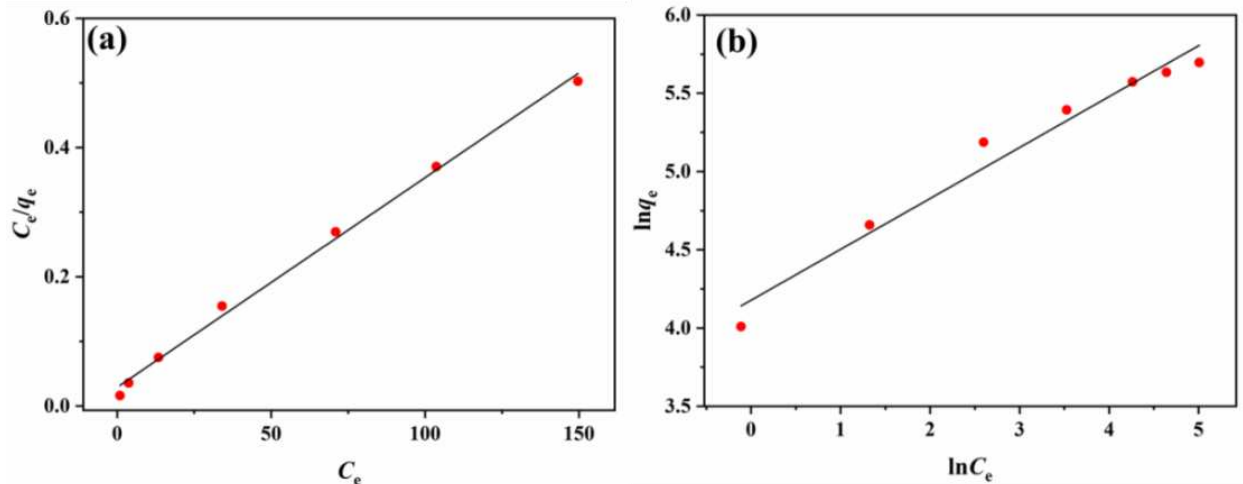
Fig. 8 a Fitting curve of the Langmuir isotherm adsorption equation, **b** fitting curve of the Freundlich adsorption isotherm equation

The fitting curves from Langmuir/Freundlich isothermal models Eq. 9-10 are shown in Fig. 8, and the fitting parameters are summarized in Table 2. The Langmuir isothermal correlation coefficient (R^2) is 0.996, and 0.971 for the Freundlich isothermal correlation coefficient. This is an indication that the adsorption of CR-SO$_3$Na by the HEC/Fe$_3$O$_4$ occurs mainly by a monolayer homogeneous adsorption process on a homogeneous adsorbent surface, and meanwhile exists a multilayer adsorption process on a heterogeneous surface. R_L is 0.029-0.24, indicating that the adsorption process is easy to occur. n is 3.075, indicating a multilayer adsorption process on a heterogeneous surface.

Table 2 Fitting isothermal parameters for the adsorption of CR-SO$_3$Na by the HC/Fe$_3$O$_4$

Langmuir				Freundlich		
R^2	K_L (L mg^{-1})	q_{max} (mg g^{-1})	R_L	R^2	K_F	n
0.996	0.1115	308.64	0.029-0.24	0.971	65.2	3.075

Adsorption temperature effect and Thermodynamics

The equilibrium adsorption capacity of the HC/Fe$_3$O$_4$ towards CR-SO$_3$Na decreases with temperature, suggesting that the adsorption of CR-SO$_3$Na on the HC/Fe$_3$O$_4$ is an exothermic process, and low temperature is more conducive to the adsorption of CR-SO$_3$Na on the HC/Fe$_3$O$_4$ (González-López et al. 2021).
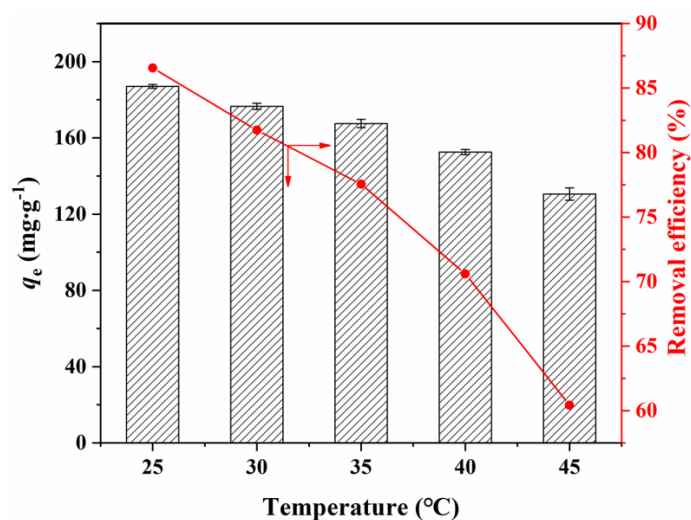
The thermodynamic parameters Gibbs free energy (ΔG^0), enthalpy change (ΔH^0) and entropy change (ΔS^0) allow to know the spontaneity, occurrence with absorption or release of energy and increase or decrease in entropy of the adsorption process from point of the thermodynamic (Ai et al. 2011, Vieira et al. 2012). The thermodynamic behavior of the adsorption of CR-SO₃Na by the HC/Fe₃O₄ were investigated using Eq. 12-14 (Ai et al. 2011, Vieira et al. 2012):

$$K_d = \frac{q_e}{c_e} \tag{12}$$

$$\ln K_d = \frac{\Delta S^0}{R} - \frac{\Delta H^0}{RT} \tag{13}$$

$$\Delta G^0 = -RT \ln K_d \tag{14}$$

where, q_e (mg g⁻¹) and C_e (mg g⁻¹) stand for the adsorption amount and CR-SO₃Na concentration at equilibrium, respectively. R (8.314 J mol⁻¹ K⁻¹) is the ideal gas constant. T (K) represents the absolute temperature.

The thermodynamic parameters calculated using Eq. 12-14 are shown in Table 3. Negative ΔG^0 values identify the spontaneity of the adsorption of CR-SO₃Na by the HC/Fe₃O₄. Positive ΔH^0 value confirms exothermic nature of the adsorption of CR-SO₃Na by the HC/Fe₃O₄. Negative ΔS^0 value demonstrates a poor affinity of the
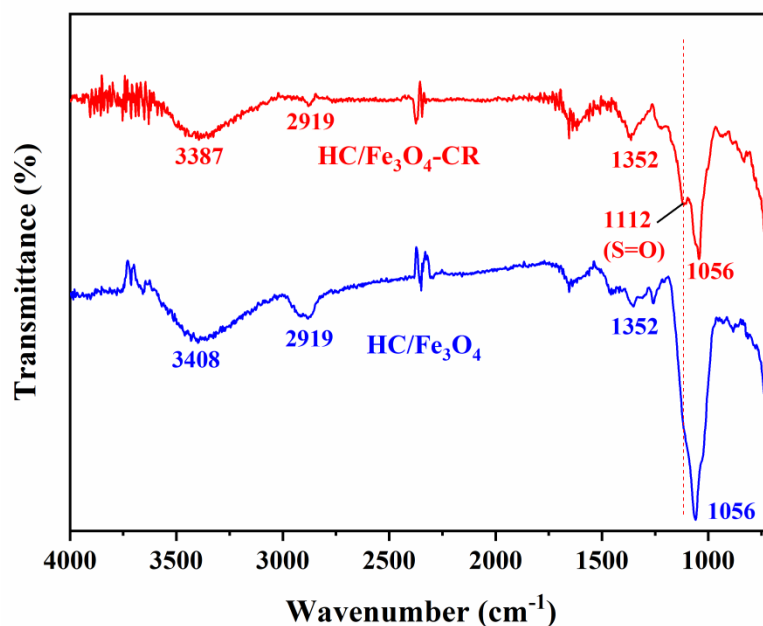
HC/Fe$_3$O$_4$ towards CR-SO$_3$Na and decreased randomness at the solid/solution interface

during adsorption process of CR-SO$_3$Na by the HC/Fe$_3$O$_4$ (Vieira et al. 2012).

Table 3 Fitting thermodynamic parameters of the adsorption of CR-SO$_3$Na by the HC/Fe$_3$O$_4$

T (K)	ΔG^0 (kJ mol^{-1})	ΔH^0 (kJ mol^{-1})	ΔS^0 (J (mol K)$^{-1}$)
298.15	-6.33		
303.15	-5.52		
308.15	-4.95	-55.06	-157.97
313.15	-4.08		
318.15	-2.95		

Possible adsorption mechanism

In order to investigate the possible adsorption mechanism of CR-SO$_3$Na by the

HC/Fe$_3$O$_4$, FT-IR spectra of the HC/Fe$_3$O$_4$ before and after CR-SO$_3$Na adsorption were

determined and shown in Fig. 10. For the convenience of understanding, the adsorbent

after CR-SO$_3$Na adsorption is named as HC/Fe$_3$O$_4$-CR-SO$_3$Na. After the adsorption of

CR-SO$_3$Na by the HC/Fe$_3$O$_4$, a new characteristic band attributed to the SO$_3^-$ group of

CR-SO$_3$Na was observed at 1112 cm^{-1} (Bai et al. 2020), confirming that CR-SO$_3$Na is

successfully adsorbed by the HC/Fe$_3$O$_4$. The absorption peak at about 3408 cm^{-1}

corresponding to the stretching vibration of the hydroxyl group of the HC/Fe$_3$O$_4$ was

apparently weakened and red-shifted. This is because after the HC/Fe$_3$O$_4$ adsorbs CR-

SO$_3$Na molecules, the H atom of the OH group on the HC/Fe$_3$O$_4$ interacts with the O

atom of the SO$_3^-$ group or the N atom of the NH$_2$ group of CR-SO$_3$Na, this interaction

results in an elongation of the O–H bond on the HC/Fe$_3$O$_4$, generating the red-shift of

the stretching vibration of O–H (Jiang et al. 2022). It is also found that the absorption

peaks at 2919, 1352, 1056 cm^{-1} keep almost invariable, indicating that the OH group on

the HC/Fe$_3$O$_4$ play an important role in the adsorption of CR-SO$_3$Na moolecules.

Fig. 10 FT-IR spectra of the HC/Fe$_3$O$_4$ before and after the adsorption of CR-SO$_3$Na

To further help understand how CR-SO$_3$Na was adsorbed by the HC/Fe$_3$O$_4$, Fig. 11 shows the schematic diagram of the possible interaction of the HC/Fe$_3$O$_4$ with CR-SO$_3$Na.   The adsorption of CR-SO$_3$Na by the HC/Fe$_3$O$_4$ primarily results from the following interactions. Firstly, the hydrogen bond interactions between the hydroxyl groups on the HC/Fe$_3$O$_4$ and CR-SO$_3$Na molecules facilitate the adsorption of CR-SO$_3$Na (Jiang et al. 2022, Xu et al. 2019). Secondly, the electrostatic interaction between CR-SO$_3$Na molecule and the HC/Fe$_3$O$_4$ is also an important driving force for the adsorption of CR-SO$_3$Na. For example, the protonated hydroxy groups on the HC/Fe$_3$O$_4$ under acidic conditions can generate electrostatic attraction towards to SO$_3^-$ of CR-SO$_3$Na, the negative OH$^-$ on the HC/Fe$_3$O$_4$ under acidic conditions can generate electrostatic repulsion towards to SO$_3^-$ of CR-SO$_3$Na. This is why acidic conditions are favorable to CR-SO$_3$Na adsorption, but not alkaline conditions (see Fig. 5a-b). Finally, the   interaction between the HC/Fe$_3$O$_4$ and the aromatic ring of CR-SO$_3$Na is beneficial to CR-SO$_3$Na adsorption (Chaukura et al. 2017).
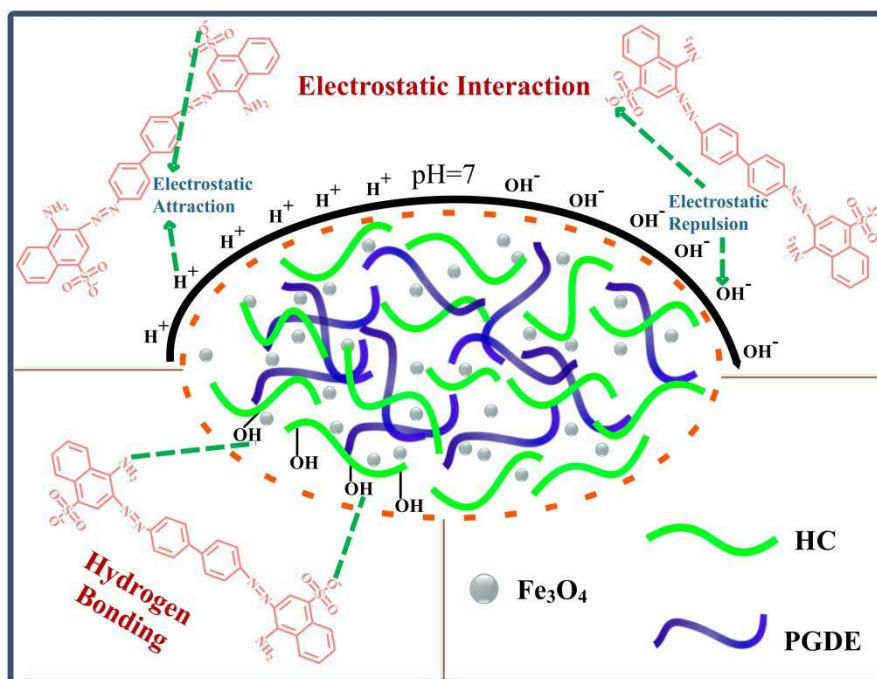
Fig. 11 Schematic diagram of the possible interaction of CR-SO$_3$Na molecules with the HC/Fe$_3$O$_4$

Conclusions

The magnetic HC/Fe$_3$O$_4$ spherical materials with porous property, an efficient adsorption capacity of CR-SO$_3$Na and an good reusability were developed, which were readily fabricated via simply mixing HC and PGDE in NaOH aqueous solution followed by subsequent introduce of Fe$_3$O$_4$ at ambient temperature. The adsorption process could be well described by the pseudo-second-order kinetic model instead of the pseudo-first-order kinetic model, and the intraparticle diffusion of CR-SO$_3$Na from the exterior surface to the interior surface of the HC/Fe$_3$O$_4$ was the rate-controlling step. CR-SO$_3$Na was adsorbed by the HEC/Fe$_3$O$_4$ mainly by a monolayer homogeneous adsorption process on a homogeneous adsorbent surface, and a multilayer adsorption process on a heterogeneous surface meanwhile also took place. The adsorption of CR-SO$_3$Na by the HC/Fe$_3$O$_4$ was a exothermic and spontaneous process as well as a decreased randomness at the solid/solution interface based on thermodynamic analysis.

The adsorption of CR-SO$_3$Na by the HC/Fe$_3$O$_4$ mainly results from the following contributions such as the hydrogen bond interactions of the HC/Fe$_3$O$_4$ with CR-SO$_3$Na molecules and the electrostatic interaction between CR-SO$_3$Na molecules and the HC/Fe$_3$O$_4$. It is expected that this work can provide valuable information for the facile fabrication of novel ecofriendly, low price and efficient adsorbent materials for removing dye pollutants from wastewaters.

References

Afkhami A, Moosavi R (2010) Adsorptive removal of Congo red, a carcinogenic textile dye, from aqueous solutions by maghemite nanoparticles. J Hazard Mater 174: 398-403

512 Afzal A, Khaliq Z, Ahmad S, Ahmad F, Noor A, Qadir MB (2021) Development and

513 characterization of biodegradable composite film. Environ Technol Inno 23:

514 101664

515 Ai LH, Li M, Li L (2011) Adsorption of Methylene Blue from Aqueous Solution with

516 Activated Carbon/Cobalt Ferrite/Alginate Composite Beads: Kinetics, Isotherms,

517 and Thermodynamics. J Chem Eng Data 56: 3475-3483

518 Al-Shemy MT, Al-Sayed A, Dacrory S (2022) Fabrication of sodium alginate/graphene

519 oxide/nanocrystalline cellulose scaffold for methylene blue adsorption: Kinetics

520 and thermodynamics study. Sep Purif Technol 290: 120825

521 Ayouch I, Kassem I, Kassab Z, Barrak I, Barhoun A, Jacquemin J, El Achaby M (2021)

522 Crosslinked carboxymethyl cellulose-hydroxyethyl cellulose hydrogel films for

523 adsorption of cadmium and methylene blue from aqueous solutions. Surf

524 Interfaces 24: 101124

525 Bai H, Chen J, Wang Z, Wang L, Lamy E (2020) Simultaneous Removal of Organic

526 Dyes from Aqueous Solutions by Renewable Alginate Hybridized with Graphene

527 Oxide. J Chem Eng Data 65: 4443-4451

528 Bhattacharyya KG, Sharma A (2004) Azadirachta indica leaf powder as an effective

529 biosorbent for dyes: a case study with aqueous congo red solutions. J Environ

530 Manage 71: 217-229

531 Chaukura N, Mamba BB, Mishra SB (2017) Conversion of Post Consumer Waste

532 Polystyrene into a High Value Adsorbent and its Sorptive Properties for Congo

533 Red Removal from Aqueous Solution. J Environ Management 193:280-289

534 Chen Y, Hanshe M, Sun Z, Zhou Y, Mei C, Duan G, Jiang S (2022) Lightweight and

535 anisotropic cellulose nanofibril/rectorite composite sponges for efficient dye

536 adsorption and selective separation. Int J Biol Macromol 207: 130-139

537   Chen Y, Long Y, Li Q, Chen X, Xu X (2019) Synthesis of High-performance Sodium

538   Carboxymethyl Cellulose-based Adsorbent for Effective Removal of Methylene

539   Blue and Pb (ii). Int J Biol Macromol 126: 107-117

540   Chronakis IS, Egermayer M, Piculell L (2002) Thermoreversible gels of

541   hydrophobically modified hydroxyethyl cellulose cross-linked by amylose.

542   Macromolecules 35: 4113-4122

543   Dai H, Huang Y, Huang H (2018) Eco-friendly Polyvinyl Alcohol/Carboxymethyl

544   Cellulose Hydrogels Reinforced with Graphene Oxide and Bentonite for

545   Enhanced Adsorption of Methylene Blue. Carbohydr Polym 185: 1-11

546   Debnath S, Ballav N, Maity A, Pillay K (2015) Development of a polyaniline-

547   lignocellulose composite for optimal adsorption of Congo red. Int J Biol

548   Macromol 75: 199-209

549   Deng J, Lei B, He A, Zhang X, Ma L, Li S, Zhao C (2013) Toward 3D graphene oxide

550   gels based adsorbents for high-efficient water treatment via the promotion of

551   biopolymers. J Hazard Mater 263: 467-478

552   Ding C, Li Y, Wang Y, Li J, Sun Y, Lin Y, Luo C (2018) Highly selective adsorption of

553   hydroquinone by hydroxyethyl cellulose functionalized with magnetic/ionic liquid.

554   Int J Biol Macromol 107: 957-964

555   Eltaweil AS, Elgarhy GS, El-Subruiti GM, Omer AM (2020) Carboxymethyl

556   cellulose/carboxylated graphene oxide composite microbeads for efficient

557   adsorption of cationic methylene blue dye. Int J Biol Macromol 154: 307-318

558   Fan HL, Li L, Zhou SF, Liu YZ (2016) Continuous preparation of Fe_3O_4 nanoparticles

559   combined with surface modification by L-cysteine and their application in heavy

560   metal adsorption. Ceram Int 42: 4228-4237

561   Feng C, Ren P, Huo M, Dai Z, Liang D, Jin Y, Ren F (2020) Facile synthesis of

562   trimethylammonium grafted cellulose foams with high capacity for selective

563   adsorption of anionic dyes from water. Carbohyd polym 241: 116369

564 Gao ZZ, Qi N, Chen WJ, Zhao H (2022) Construction of Hydroxyethyl

565   Cellulose/Silica/Graphitic Carbon Nitride Solid Foam for Adsorption and

566   Photocatalytic Degradation of Dyes. Arab J Chem 2022: 104105

567 Gautam RK, Mudhoo A, Chattopadhyaya MC (2013) Kinetic, equilibrium,

568   thermodynamic studies and spectroscopic analysis of Alizarin Red S removal by

569   mustard husk. J Environ. Chem Eng 1: 1283-1291

570 González-López ME, Laureano-Anzaldo CM, Pérez-Fonseca AA, Gómez C, Robledo-

571   Ortíz JR (2021) Congo red adsorption with cellulose-graphene nanoplatelets beads

572   by differential column batch reactor. J Environ Chem Eng 9: 105029

573 Helmiyati H, Fitriana N, Chaerani ML, Dini FW (2022) Green hybrid photocatalyst

574   containing cellulose and γ-Fe_2O_3-ZrO_2 heterojunction for improved visible-light

575   driven degradation of Congo red. Opt Mater 124: 111982

576 Hirosawa K, Fujii K, Hashimoto K, Shibayama M (2017) Solvated Structure of

577   Cellulose in a Phosphonate-Based Ionic Liquid. Macromolecules 50: 6509−6517

578 Hosseini H, Zirakjou A, McClements DJ, Goodarzi V, Chen WH (2022) Removal of

579   methylene blue from wastewater using ternary nanocomposite aerogel systems:

580   Carboxymethyl cellulose grafted by polyacrylic acid and decorated with graphene

581   oxide. J Hazard Mater 421: 126752

582 Huang S, Wu L, Li T, Xu D, Lin X, Wu C (2019) Facile preparation of biomass lignin-

583   based hydroxyethyl cellulose super-absorbent hydrogel for dye pollutant removal.

584   Int J Biol Macromol 137: 939-947

585 Huo Y, Liu Y, Yang J, Du H, Qin C, Liu H (2022) Polydopamine-Modified Cellulose

586   Nanofibril Composite Aerogel: An Effective Dye Adsorbent. Langmuir 38: 4164-

587 4174

588 Jiang X, Xue J, Zhang Y, Xiong Z, Zhao L (2022) Facile synthesis of DTC-Chm-GO

589   nanocomposite with remarkable adsorption capacity and antibacterial activity.

590   Mater Sci Eng B, 2022, 275: 115517

591 Jilal I, El Barkany S, Bahari Z, Sundman O, El Idrissi A, Abou-Salama M, Amhamdi H

592   (2018) New quaternized cellulose based on hydroxyethyl cellulose (HEC) grafted

593   EDTA: synthesis, characterization and application for Pb (II) and Cu (II) removal.

594   Carbohyd polym 180: 156-167

595 Law KL, Morét-Ferguson SE, Goodwin DS, Zettler ER, DeForce E, Kukulka T,

596   Proskurowski G (2014) Distribution of surface plastic debris in the eastern Pacific

597   Ocean from an 11-year data set. Environ Sci Technol 48: 4732-4738

598 Li Y, Xiao H, Pan Y, Wang L (2018) Novel composite adsorbent consisting of dissolved

599   cellulose fiber/microfibrillated cellulose for dye removal from aqueous solution.

600   ACS Sustain Chem Eng 6: 6994-7002

601 Liu L, Gao ZY, Su XP, Chen X, Jiang L, Yao JM (2015) Adsorption removal of dyes

602   from single and binary solutions using a cellulose-based bioadsorbent. ACS

603   Sustain Chem Eng, 2015, 3: 432-442

604 Oyewo OA, Adeniyi A, Sithole BB, Onyango MS (2020) Sawdust-based cellulose

605   nanocrystals incorporated with ZnO nanoparticles as efficient adsorption media in

606   the removal of methylene blue dye. ACS omega 5: 18798-18807

607 Patel K, Chikkali SH, Sivaram S (2020) Ultrahigh molecular weight polyethylene:

608   Catalysis, structure, properties, processing and applications. Plog Polym SCI 109:

609   101290

610 Pavan FA, Camacho ES, Lima EC, Dotto GL, Branco VT, Dias SL (2014) Formosa

611   papaya seed powder (FPSP): preparation, characterization and application as an

612   alternative adsorbent for the removal of crystal violet from aqueous phase. J

613   Environ Chem Eng 2: 230-238

614 Ragauskas AJ, Williams CK, Davison BH, Britovsek G, Cairney J, Eckert CA,

615   Tschaplinski T (2006) The Path Forward for Biofuels and Biomaterials. Sci

616   311:484−489

617 Rillig MC (2012) Microplastic in terrestrial ecosystems and the soil? Environment 46:

618   6453-6454

619 Roa K, Oyarce E, Boulett A, ALSamman M, Oyarzún D, Pizarro GDC, Sánchez J (2021)

620   Lignocellulose-based materials and their application in the removal of dyes from

621   water: A review. Sustain Mater Techno 29: e00320

622 Robinson T, Chandran B, Nigam P (2002) Effect of pretreatments of three waste

623   residues, wheat straw, corncobs and barley husks on dye adsorption. bioresource

624   technol 85: 119-124

625 Roy A, Chakraborty S, Kundu SP, Adhikari B, Majumder SB (2012) Adsorption of

626   anionic-azo dye from aqueous solution by lignocellulose-biomass jute fiber:

627   equilibrium, kinetics, and thermodynamics study. Ind Eng Chem Res 51: 12095-

628   12106

629 Shafik AL, Hashem MA, El Sayed M (2022) Rapid adsorption of acid dyes using Cu

630   (II) thiourea modified cellulose complex. Int J Biol Macromol 205: 692-702

631 Shi H, Li W, Zhong L, Xu C (2014) Methylene blue adsorption from aqueous solution

632   by magnetic cellulose/graphene oxide composite: equilibrium, kinetics, and

633   thermodynamics. Ind Eng Chem Res 53: 1108-1118

634 Sirajudheen P, Nikitha MR, Karthikeyan P, Meenakshi S (2020) Perceptive removal of

635   toxic azo dyes from water using magnetic Fe_3O_4 reinforced graphene oxide-

636   carboxymethyl cellulose recyclable composite: Adsorption investigation of

637   parametric studies and their mechanisms. Surf Interfaces 21: 100648

638   Siró I, Plackett D (2010) Microfibrillated cellulose and new nanocomposite materials:

639   a review. Cellulose 17: 459-494

640   Sultan M, Nagieb ZA, El-Masry HM, Taha GM (2022) Physically-crosslinked

641   hydroxyethyl cellulose-g-poly (acrylic acid-co-acrylamide)-Fe^{3+}/silver

642   nanoparticles for water disinfection and enhanced adsorption of basic methylene

643   blue dye. Int J Biol Macromol 196: 180-193

644   Verma M, Tyagi I, Kumar V, Goel S, Vaya D, Kim H (2021) Fabrication of GO-MnO2

645   nanocomposite using hydrothermal process for cationic and anionic dyes

646   adsorption: Kinetics, isotherm, and reusability. J Environ Chem Eng 9: 106045

647   Vieira SS, Magriotis ZM, Santos NAV, das Gracas Cardoso M, Saczk AA (2012)

648   Macauba palm (Acrocomia aculeata) cake from biodiesel processing: an efficient

649   and low cost substrate for the adsorption of dyes. Chem Eng J 183: 152-161

650   Wan Y, Liu ZY, Song P, Zhang XQ, Song JC, Fu YJ, Shi CY (2019) Ionic liquid groups

651   modified 3D porous cellulose microspheres for selective adsorption of AO7 dye.

652   J Clean Prod 240: 118201

653   Wang H, Gurau G, Rogers RD (2012) Ionic liquid Processing of Cellulose. Chem Soc

654   Rev 41: 1519−1537

655   Wang Z, Song L, Wang Y, Zhang XF, Yao J (2021) Construction of a Hybrid Graphene

656   Oxide/Nanofibrillated Cellulose Aerogel used for the Efficient Removal of

657   Methylene Blue and Tetracycline. J Phys Chem Solids 150, 109839

658   Wu J, Andrews MP (2020) Carboxylated cellulose nanocrystal microbeads for removal

659   of organic dyes from wastewater: effects of kinetics and diffusion on binding and

660   release. ACS Appl Nano Mater 3: 11217-11228

661   Xu AR, Chen L, Guo X, Xiao Z, Liu R (2018) Biodegradable lignocellulosic porous

662   materials: fabrication, characterization and its application in water processing. Int

663   J Biol Macromol 115: 846-852

664   Xu AR, Chen L, Wang J (2018) Functionalized imidazalium carboxylates for enhancing

665   practical applicability in cellulose processing. Macromolecules 51: 4158-4166

666   Xu AR, Wang F (2020) Carboxylate Ionic Liquid Solvent Systems from 2006 to 2020:

667   Thermal Properties and Application in Cellulose Processing. Green Chem 22:

668   7622-7664

669   Xu AR, Wang W, Duo T, Wang Y, Xiao Z, Liu R (2022) High-performance

670   polyethyleneimine/sodium silicate material: One-step strategy at ambient

671   temperature and application in removing heavy metal ion. J Mater Sci 57: 4221-

672   4238

673   Xu AR, Wang Y, Gao J, Wang J (2019) Facile fabrication of a homogeneous

674   cellulose/polylactic acid composite film with improved biocompatibility,

675   biodegradability and mechanical properties. Green Chem 21: 4449-4456

676   Yuan HB, Tang RC, Yu CB (2022) Microcrystalline cellulose modified by phytic acid

677   and condensed tannins exhibits excellent flame retardant and cationic dye

678   adsorption properties. Ind Crops Prod 184: 115035

679   Zaman A, Orasugh JT, Banerjee P, Dutta S, Ali MS, Das D, Chattopadhyay D (2020)

680   Facile one-pot in-situ synthesis of novel graphene oxide-cellulose nanocomposite

681   for enhanced azo dye adsorption at optimized conditions. Carbohyd polym 246:

682   116661

683   Zhang LN, Ruan D, Gao SJ (2002) Dissolution and regeneration of cellulose in

684   NaOH/thiourea aqueous solution. J Polym Sci Part B: Polym 40, 1521-1529

685   Zhang W, Wang L, Mäkilä E, Willför S, Xu C (2022) Ultralight and porous cellulose

686   nanofibers/polyethyleneimine composite aerogels with exceptional performance

687   for selective anionic dye adsorption. Ind Crops Prod 177: 114513

688   Zhou Y, Zhang M, Hu X, Wang X, Niu J, Ma T (2013) Adsorption of cationic dyes on

689   a cellulose-based multicarboxyl adsorbent. J Chem Eng Data 58: 413-421

690